Article

Anomalous Dome-like Superconductivity in RE$_2$(Cu$_{1-x}$Ni$_x$)$_5$As$_3$O$_2$ (RE = La, Pr, Nd)

Xu Chen,
Jiangang Guo,
Chunsheng
Gong, ...,
Jiangping Hu,
Shiyan Li,
Xiaolong Chen

jgguo@iphy.ac.cn (J.G.)
chenx29@iphy.ac.cn (X.C.)

HIGHLIGHTS

We discover three new layered superconductors Ni-doped RE$_2$Cu$_5$As$_3$O$_2$ (RE = La, Pr, Nd)

Superconductivity is related to a new kind of [Cu$_5$As$_3$]$^{2-}$ unit

Substituting Cu by Ni induces anomalously dome-like T_c and variation of As-As covalent

iScience

Article

Anomalous Dome-like Superconductivity in $RE_2(Cu_{1-x}Ni_x)_5As_3O_2$ (RE = La, Pr, Nd)

Xu Chen,[1,2,7] Jiangang Guo,[1,7,8,*] Chunsheng Gong,[1] Erjian Cheng,[3] Congcong Le,[1,4] Ning Liu,[1,2] Tianping Ying,[3] Qinghua Zhang,[1] Jiangping Hu,[1,4,6] Shiyan Li,[3,5] and Xiaolong Chen[1,2,6,*]

SUMMARY

A significant manifestation of interplay of superconductivity and charge density wave, spin density wave, or magnetism is a dome-like superconducting critical temperature (T_c) in cuprate, iron-based, and heavy Fermion superconductors. Pesudogap, quantum critical point, and strange metals emerge in different doping ranges. Exploring dome-like T_c in new superconductors is of interest to detect emergent effects. Here we report the superconductivity in a new layered Cu-based compound $RE_2Cu_5As_3O_2$ (RE = La, Pr, Nd), in which the T_c exhibits dome-like variation with a maximum T_c of 2.5, 1.2, and 1.0 K with substitution of Cu by large amount of Ni ions. Simultaneously, the structural parameters like As-As bond length and c/a ratio exhibit unusual variations as the Ni-doping level goes through the optimal value. The robustness of superconductivity, up to 60% of Ni doping, reveals the unexpected impurity effect on inducing and enhancing superconductivity in these novel layered materials.

INTRODUCTION

Cuprate superconductors are a class of layered compounds that belong to the regime of strongly correlated electron system, and their superconducting energy gaps are thought to be *d*-wave type (Wollman et al., 1993; Tsuei and Kirtley, 2000). Both magnetic and non-magnetic impurities in the Cu site will seriously suppress superconductivity (SC) (Xiao et al., 1990). Dome-like T_c often shows up when the carrier concentration increases from 5% to 25% by doping in non-CuO₂ layers (spacer layers) (Lee et al., 2006). For iron-based superconductors, carrier change by doping in non-SC layers may have a similar effect on T_c, but the effect of impurities on the Fe site is totally different, which is regarded as a signature of different superconducting gap symmetry details, S +- (Mazin, 2010; Mazin et al., 2008) or S++ (Kuroki et al., 2008; Onari and Kontani, 2009). For example, partial substitution of O by F in LaFeAsO (Kamihara et al., 2008) or Ba by K in BaFe₂As₂ (Rotter et al., 2008) can lead to the dome-like T_c. Surprisingly, similar dome-shaped T_c can also be achieved by substituting Fe^{2+} by Co^{2+} or Ni^{2+} ions with more 3*d* electrons (Sefat et al., 2008; Canfield et al., 2009; Ni et al., 2010; Li et al., 2009). One explanation is that the doping is justified by the rigid-band model to some extent, where the doped electrons are in itinerant states, only shifting the Fermi level to the higher density of states (Ideta et al., 2011, 2013). At the same time, the correlation strength of electrons and spin fluctuations might be drastically modified (Nakajima et al., 2014; Dai et al., 2012). As far as we know, such dome-like T_c induced by Ni^{2+} has not been known in other systems.

In this work, we report three novel layered superconductors, $RE_2Cu_5As_3O_2$ (RE = La, Pr, Nd), where Cu is coordinated by As in a new kind of $[Cu_5As_3]^{2-}$ block. $La_2Cu_5As_3O_2$ (La2532) shows superconducting transition at T_c = 0.63 K, whereas Pr2532 and Nd2532 are non-superconducting phases. Strikingly, dome-like T_c emerges in $RE_2(Cu_{1-x}Ni_x)_5As_3O_2$ upon a wide range of Ni doping (0 < *x* < 0.6). These series of compounds exhibit different superconducting evolutions from both cuprate and iron-based superconductors. Our results highlight the role of Ni doping coupled with structural anomaly in inducing SC with Landau-Fermi liquid behavior.

RESULTS

Figure 1A shows the high-angle annular dark-field image of the (110) plane of La2532, in which two different slabs stack along the *c*-axis, indicating a typical layered structure. The collected powder X-ray diffraction (PXRD) pattern of La2532 can be indexed by a body-centered tetragonal cell with space group *I*4/*mmm* (No. 139). The refined lattice constants are *a* = *b* = 4.1386(1) Å and *c* = 22.8678(6) Å. We construct the initial model by setting La1 4e (0.5, 0.5, z1), O1 4d (0.5, 0, 0.25), Cu(1) 8g (0.5, 0, z2), Cu(2) 2b (0, 0, 0.5), As(1) 4e
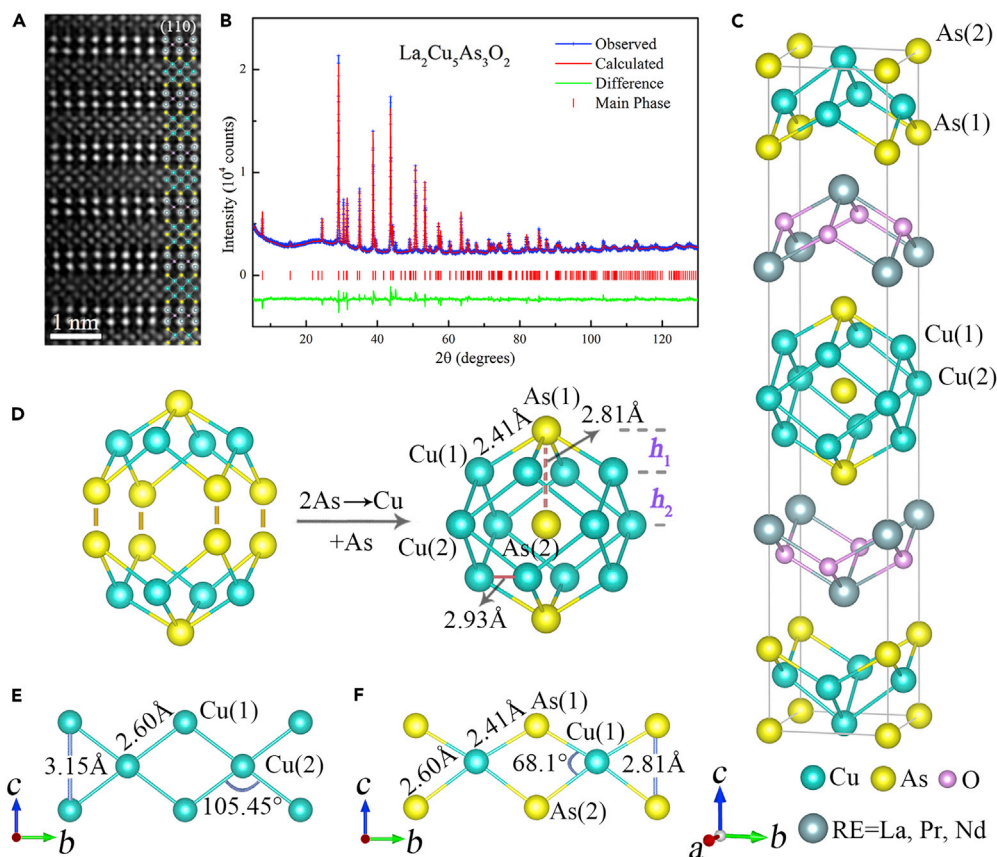
Figure 1. Structural Determination, Crystal Structure, and Bonding Details of RE$_2$Cu$_5$As$_3$O$_2$

(A) High-angle annular dark-field image of (110) plane of La$_2$Cu$_5$As$_3$O$_2$.

(B) Rietveld refinement of PXRD of La2532 collected at 300 K.

(C) Crystal structure of RE$_2$Cu$_5$As$_3$O$_2$ (RE = La, Pr, Nd).

(D) [Cu$_5$As$_3$]$^{2-}$ unit is a combination of two Cu$_2$As$_2$ layers by replacing two As atoms by Cu atom. One more As atom is encapsulated in the center.

(E)Cu-Cu bond length and angle in Cu network.

(F) Cu-As bond length and angle in Cu-As fragment.

(0, 0, z3), and As(2) 2a (0, 0, 0) as per $I4/mmm$. The Rietveld refinement successfully converges to R_p = 2.95%, R_{wp} = 4.26%, and χ^2 = 3.87, and the refined patterns are shown in Figure 1B. Pr2532 and Nd2532 are found to be isostructural to La2532 with lattice parameters a = 4.0802(1) Å, c = 22.9144(5) Å and a = 4.0561(1) Å, c = 23.0082(6) Å, respectively. The crystallographic parameters of RE2532 (RE = La, Pr, Nd) are summarized in Table S1.

The crystal structure of RE2532 is drawn in Figure 1C; one can see that the [Cu$_5$As$_3$]$^{2-}$ blocks and the fluorite RE$_2$O$_2$ layers stack along the c-axis, which agrees with the atomic distributions in HADDF image and stoichiometry of energy dispersive spectrometer (EDS) analysis (Figure S1). Figure 1D provides structural detail of the [Cu$_5$As$_3$]$^{2-}$ block, which can be viewed as replacing neighbor As^{3-} anions of two Cu$_2$As$_2$ layers by one Cu atom. The bond lengths of Cu(1)-As(1) and Cu(1)-Cu(1) are 2.41 Å and 2.93 Å, respectively, close to the values in BaCu$_2$As$_2$ (Saparov and Sefat, 2012). It is noted that the bond length of As(1)-As(2), 2.81 Å, locates at the bonding regime of As-As covalent bond, 2.7–2.9 Å (Yakita et al., 2014). The [Cu$_5$As$_3$]$^{2-}$ unit is analogous to [Cu$_6$Pn$_2$]$^{2-}$ in BaCu$_6$Pn$_2$ (Pn = As, P) (Dünner and Mewis, 1995), where the central As atom is replaced by one Cu(2) atom. In Figures 1E and 1F, we can see that metallic bond of Cu-Cu exists in Cu network along the b-axis as indicated by the bond length, 2.60 Å, of Cu(1)-Cu(2). In coordination environment of Cu(1), short Cu(1)-As(1) and Cu(1)-As(2) bond lengths, 2.41 Å and 2.60 Å, suggest the covalent nature in [Cu$_5$As$_3$]$^{2-}$ unit like the Fe-As bonds in [Fe$_2$As$_2$]$^{2-}$ layers of iron-based superconductors (Huang et al., 2008).
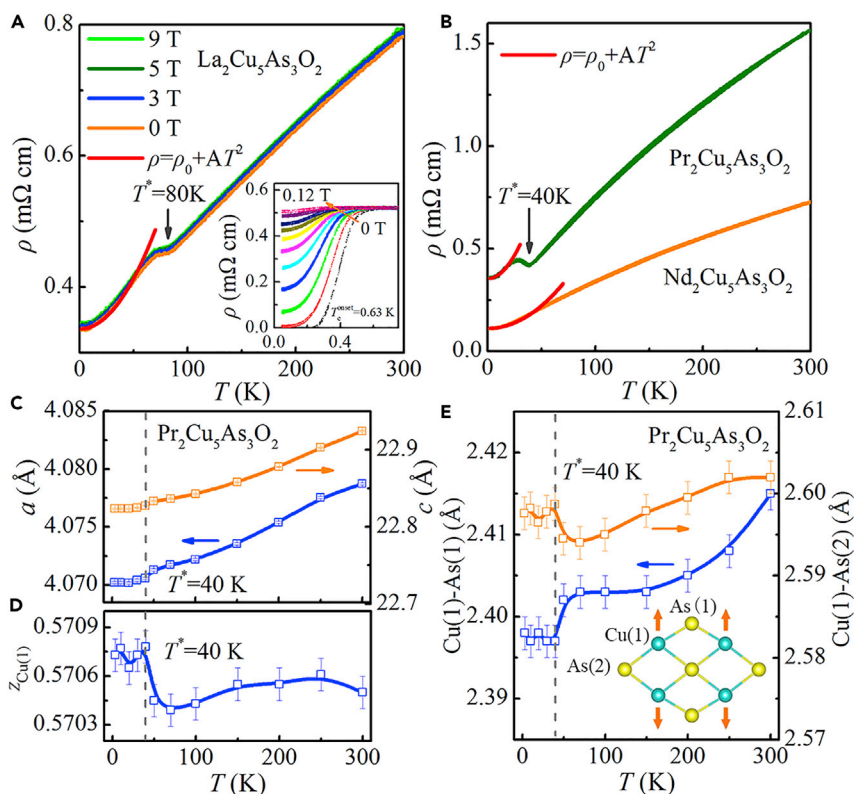
Figure 2. Transport Properties and Crystal Structure at Various Temperatures

(A) Temperature-dependent electrical resistivity of $La_2Cu_5As_3O_2$ from 1.8 K-300 K. The data below T^* are fitted by Fermi-liquid equation (red lines). The inset is the electrical resistivity of $La_2Cu_5As_3O_2$ around T_c under external magnetic field.

(B) Normal-state electrical resistivity of $RE_2Cu_5As_3O_2$ (RE=Pr, Nd) measured from 1.8 K-300 K. The data below T^* are fitted by Fermi-liquid equation (red lines).

(C) Temperature-dependent lattice constants a and c of $Pr_2Cu_5As_3O2$.

(D) Temperature-dependent atomic position of $z_{Cu(1)}$ of $Pr_2Cu_5As_3O_2$.

(E) The Cu(1)-As(1) and Cu(1)-As(2) bond lengths versus temperature. Inset shows schematic variation of Cu(1) below T^*.

The electrical resistivity of $RE_2Cu_5As_3O_2$ from 300 to 1.8 K is plotted in Figures 2A and 2B. All data exhibit metallic behaviors, which can be fitted by $\rho \sim T^2$ at low temperature range, obeying the Fermi liquid behavior; see the details in Figure S2. There are resistivity kinks for La2532 and Pr2532 at T^* = 80 and 40 K, respectively. The external magnetic fields up to 9 T do not weaken this kink. However, for Nd2532, there is no resistivity kink above 1.8 K. Measuring the resistivity at very low temperature reveals that La2532 is a superconductor with T_c^{onset} = 0.63 K and T_c^{zero} = 0.26 K, as shown in the inset of Figure 2A. The transition is suppressed by external magnetic field and finally disappears as B > 0.12 T. The upper critical fields $\mu_0 H_{c2}(0)$, 0.15 and 0.18 T, are estimated from the linear and Ginzburg-Landau (GL) fitting, respectively (Figure S3). In contrast, Pr2532 and Nd2532 are not superconductors above 0.25 K. This difference is possibly similar to the effect of suppressed SC in Pr-based cuprates (Chen et al., 1992, 1995).

The magnetic susceptibility (χ) and specific heat (C_p) at low temperatures were measured and plotted in Figure S4. The fitting of $\chi(T)$ gives the effective magnetic moment μ_{eff} = 0.16 μ_B and θ = −148(1) K, implying an anti-ferromagnetic (AFM) interaction of Cu ions. Furthermore, the fitting of C_p yields a Debye temperature Θ_D of 169(2) K and Sommerfeld coefficient γ_0 = 5.01 mJ·mol^{-1}·K^{-2} for La2532. We rule out the possibility of charge-density-wave transition by performing transmission electron microscopic imaging of La2532 at low temperature; see Figure S5. Meanwhile, the Rietveld refinement of temperature-dependent PXRD patterns of Pr2532 reveals that the a- and c-axes shrink on cooling, but both values show slight discontinuity at 40 K, implying a structural distortion; see Figures 2C and S6. In Figure 2D, it is found that the $z_{Cu(1)}$ anomaly increases below 40 K. It leads to abrupt contraction of Cu(1)-As(1) bond and elongation of Cu(1)-As(2) bond, which enhances the structural anisotropy of $[Cu_5As_3]^{2-}$, as shown in Figure 2E.

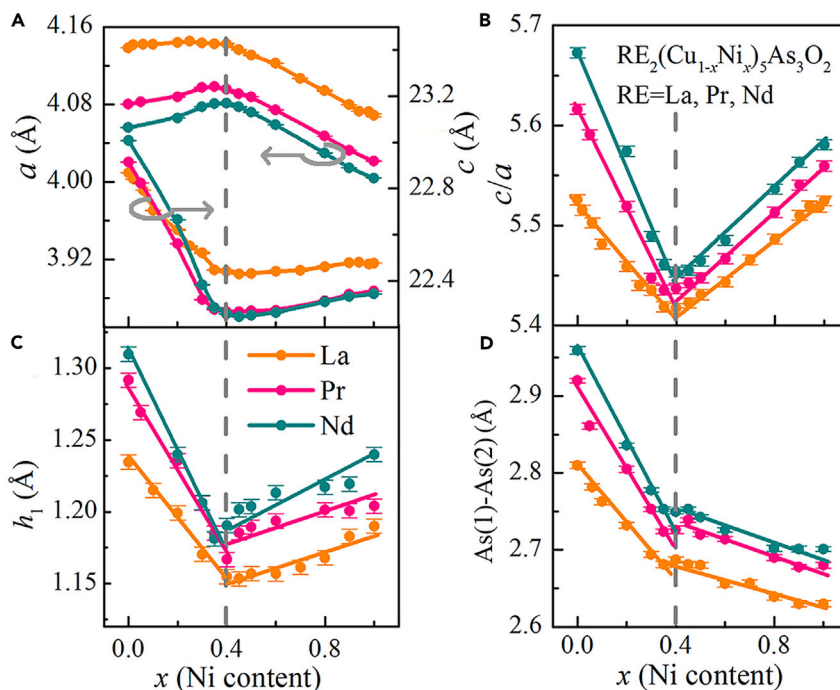**Figure 3. Selected Crystallographic Parameters of RE$_2$(Cu$_{1-x}$Ni$_x$)$_5$As$_3$O$_2$ as a Function of Ni Content**

(A) a and c.

(B) c/a ratio.

(C) As height (h_1).

(D) As(1)-As(2) bond length.

Such change could induce charge redistribution and small resistivity jump. It is similar to the structural change and resistivity jump in KNi$_2$S$_2$ (Neilson et al., 2013).

We prepared a series of RE$_2$(Cu$_{1-x}$Ni$_x$)$_5$As$_3$O$_2$ ($x = 0$–1.0) samples so as to further explore the evolution of SC against Ni substitution. The PXRD confirms that RE$_2$(Cu$_{1-x}$Ni$_x$)$_5$As$_3$O$_2$ is a continuous solid solution, judging from the linear decrease in the volume of unit cell (Figure S7). The results of Rietveld refinement for all patterns are listed in Table S1. Selected crystallographic parameters are plotted in Figure 3. One can see that the c-axis decreases drastically as $x < 0.4$, but the a-axis almost keeps constant; however, this variation is reversed as $x > 0.4$; see Figure 3A. This anomalous feature makes the c/a ratio initially decrease as $x < 0.4$, whereas it starts to increase as $x > 0.4$, where the minimum shows up at $x = 0.4$, as shown in Figure 3B. To the best of our knowledge, the structural changes of a, c, and "V" shape of c/a ratio are rare in layer superconductors. In Figure 3C, the As height (h_1) first decreases as $x < 0.4$ and then increases, where the crossover perfectly matches the structural anomaly $x = 0.4$. The h_2 only linearly decreases upon Ni doping. The distinct variations of h_1 and h_2 induce a crossover of shrunk As(1)-As(2) bond length at $x = 0.4$; see Figure 3D. On the other hand, as the Ni doping changes the coordination environment of Cu(1), and the Cu(2)-As(2) bond length ($\sqrt{2}$*a/2) almost remains constant, we speculate that the Ni first occupies the Cu(1) site as $x < 0.4$, shortening the h_1 and c-axis.

The electrical resistivities of RE$_2$(Cu$_{1-x}$Ni$_x$)$_5$As$_3$O$_2$ at low temperature are shown in Figures 4A–4C. For La$_2$(Cu$_{1-x}$Ni$_x$)$_5$As$_3$O$_2$, the T_c^{onset} monotonously increases to the maximal 2.5 K as $x = 0.4$. It is surprising that SC can be induced in the non-superconducting Pr2532 and Nd2532 by Ni doping, in which the T_c^{onset} also increases to the highest value 1.2 and 1.0 K as $x \sim 0.4$, respectively. Once x is above 0.4, the T_c^{onset} gradually decreases and finally vanishes up to 0.6. The external magnetic fields smoothly suppress the SC off, and the $\mu_0 H'_{c2}(0)$ for the three optimally doped samples are 3.8 T (3.0 T), 0.69 T (0.52 T), and 0.54 T (0.37 T) estimated from the linear (GL) fitting, respectively (Figure S8). In Figures 4D and 4E, the magnetization of three optimally doped samples exhibit large superconducting volume fractions, indicating a bulk SC. Furthermore, the bulk SC of La$_2$(Cu$_{0.6}$Ni$_{0.4}$)$_5$As$_3$O$_2$ is confirmed by a large superconducting jump in the specific
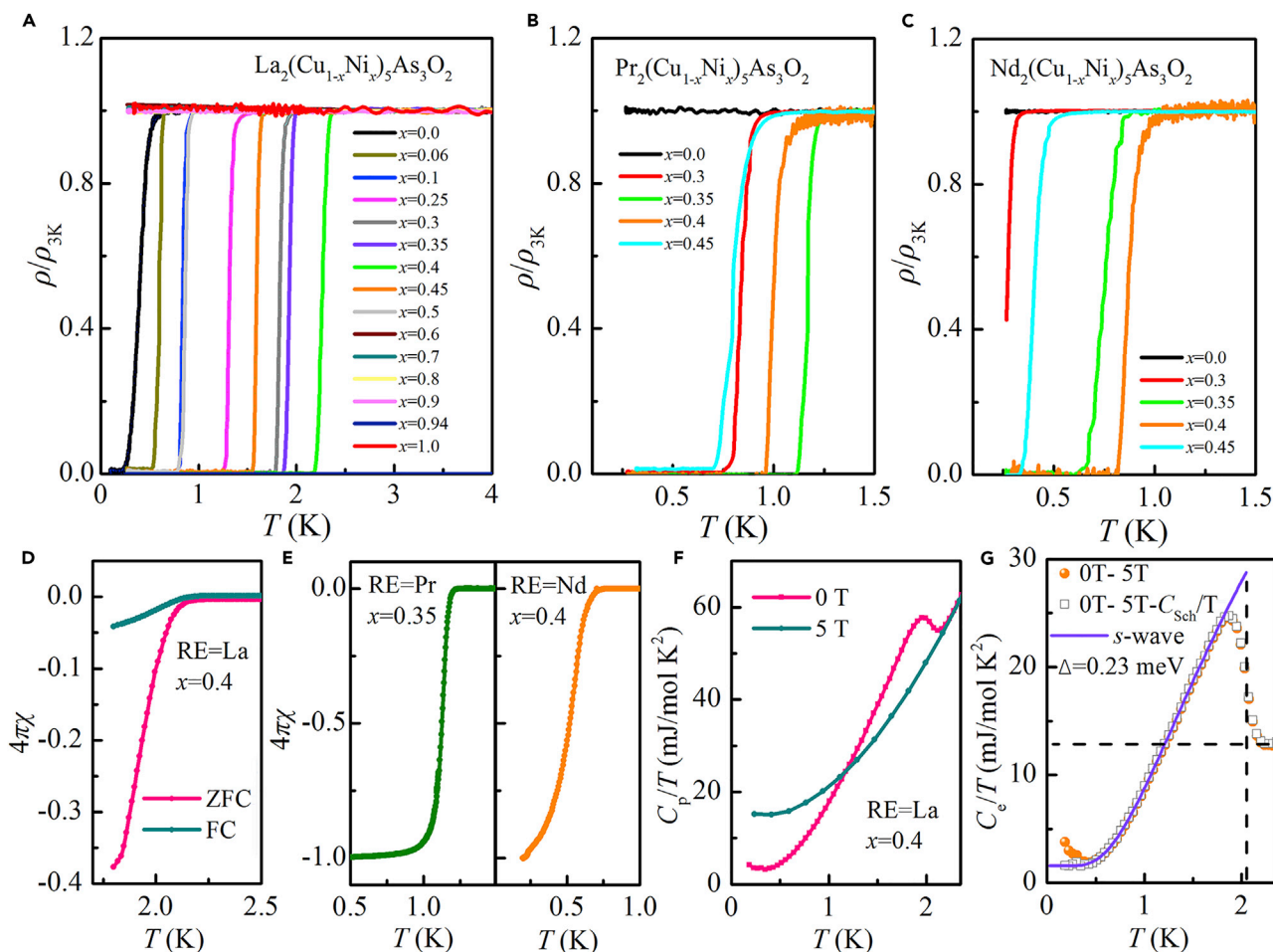
Figure 4. Physical Properties of RE$_2$(Cu$_{1-x}$Ni$_x$)$_5$As$_3$O$_2$ (RE = La, Pr, Nd)

(A) Superconducting transitions of La$_2$(Cu$_{1-x}$Ni$_x$)$_5$As$_3$O$_2$. As increasing x, the T_c exhibit similar trend that firstly increases to maximal value and then decreases.

(B) Superconducting transitions of Pr$_2$(Cu$_{1-x}$Ni$_x$)$_5$As$_3$O2.

(C) Superconducting transitions of Nd$_2$(Cu$_{1-x}$Ni$_x$)$_5$As$_3$O$_2$.

(D) Superconducting volume fractions of La$_2$(Cu$_{0.6}$Ni$_{0.4}$)$_5$As$_3$O$_2$ under H= 10 Oe.

(E) Superconducting volume fractions for Pr$_2$(Cu$_{0.65}$Ni$_{0.35}$)$_5$As$_3$O$_2$ and Nd$_2$(Cu$_{0.6}$Ni$_{0.4}$)$_5$As$_3$O$_2$ under H= 10 Oe.

(F) C_p/T of La$_2$(Cu$_{0.6}$Ni$_{0.4}$)$_5$As$_3$O$_2$ as a function of temperature under 0 T and 5 T.

(G) C_e/T and the fitting curves of La$_2$(Cu$_{0.6}$Ni$_{0.4}$)$_5$As$_3$O$_2$ against temperature.

heat (C_p). The magnetic field up to 5 T totally suppresses the SC, as seen from Figure 4F. We fit the C_p(5T) data using the equation $C_p/T = \gamma + \beta T^2$ and obtain γ = 12.62 mJ·mol^{-1}·K^{-2}, β = 9.89 mJ·mol^{-1}·K^{-4}, and Θ_D = 133(2) K. Extrapolating the data to 0 K leads to a residual γ_n 1.58 mJ·mol^{-1}·K^{-2}, indicating that the non-superconducting phase is ~12.5% due to impurity. Thus we obtain the superconducting γ_s as 11.04 mJ·mol^{-1}·K^{-2}, which results in the dimensionless jump of $C_e/\gamma_s T_c$ of 1.42; see Figure 4G. This value is consistent with the Bardeen–Cooper–Schrieffer (BCS) weak-coupling limit (1.43), but smaller than that of the optimal K-doped BaFe$_2$As$_2$ (2.5) (Popovich et al., 2010). We subtract the upturn of C_e/T at very low temperature due to Schottky anomaly using the treatment in Mu et al. (2007) and obtain the flatten C_e/T. As per the BCS theory, $C_e/T \propto \exp\left[-\frac{\Delta(0)}{k_B T}\right]$, the data are fitted, yielding superconducting gap $\Delta(0)$ = 0.23 meV = 2.65k_B K. Knowing the $\Delta(0)$, $2\Delta(0)/k_B T_c$ is 2.58, which is smaller than the weak coupling limit (3.52) within the BCS framework. The estimation of the Schottky anomaly and semi-logarithmic of C_e/T are shown in Figure S9. Note that subtracting the Schottky anomaly possibly undermines the rationality of s-wave SC.

The electrical resistivity of RE$_2$(Cu$_{1-x}$Ni$_x$)$_5$As$_3$O$_2$ from 1.8 to 300 K shows that the T^* is rapidly suppressed upon slight Ni doping (x < 0.1) as shown in Figure S10. In end member La$_2$Ni$_5$As$_3$O$_2$, Pr$_2$Ni$_5$As$_3$O$_2$, and

A

B

C
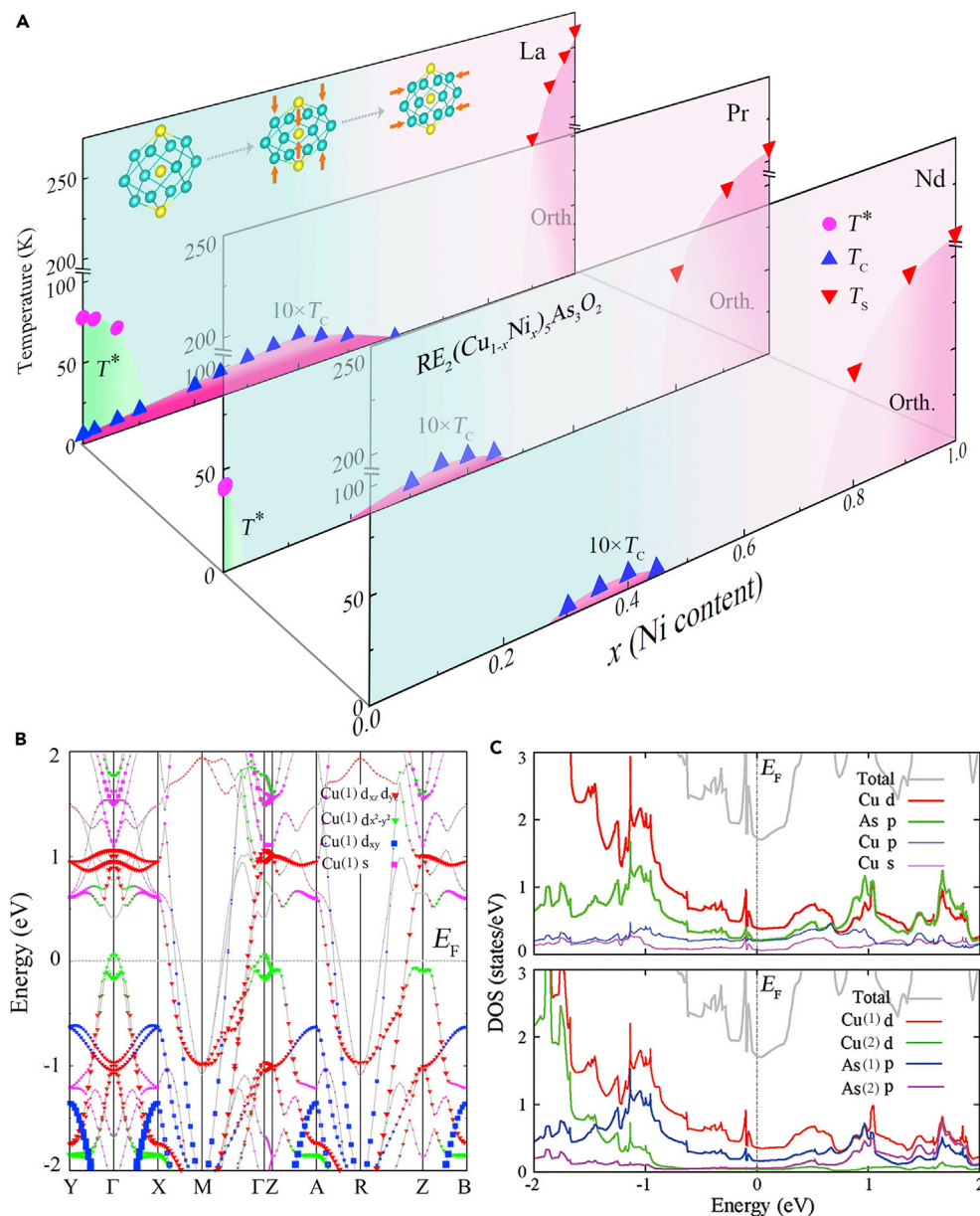
Figure 5. Phase Diagram of RE$_2$(Cu$_{1-x}$Ni$_x$)$_5$As$_3$O$_2$ and Electronic Structure of La$_2$Cu$_5$As$_3$O$_2$

(A) Phase diagram of RE$_2$(Cu$_{1-x}$Ni$_x$)$_5$As$_3$O$_2$. It can be seen that the T^* is suppressed and dome-like T_c shows up. The inset shows that the structure of [Cu$_5$As$_3$]$^{2-}$ unit changes upon Ni doping.

(B) Cu(1) orbital-weighted band structures of La$_2$Cu$_5$As$_3$O$_2$.

(C) Upper panel: the projected density of states of Cu d, p, s, and As p orbitals at the ranges of −2 to 2 eV. Lower panel: the projected density of states of different Cu and As site, showing the Cu(1) d and As(1) p orbitals dominate at the Fermi level.

Nd$_2$Ni$_5$As$_3$O$_2$, another resistivity anomaly associated with structural transition shows up, where the T_s are 260, 210, and 190 K, respectively. Indexing temperature-dependent PXRD patterns of La$_2$(Cu$_{0.02-}$Ni$_{0.98}$)$_5$As$_3$O$_2$ found that the (200) and (215) peaks split into (020)/(200) and (125)/(215) peaks below T_s, indicating a symmetry breaking from tetragonal (C_4) to orthorhombic phase (C_2, $Immm$, No. 71) (Figure S11). We can map out the electronic phase diagram of RE$_2$(Cu$_{1-x}$Ni$_x$)$_5$As$_3$O$_2$; see Figure 5A. The most interesting thing is that dome-like T_c can be observed, where the superconducting phases emerge at $0 < x < 0.6$, $0.2 < x < 0.45$, and $0.3 < x < 0.45$ for Ni-doped La2532, Pr2532, and Nd2532, respectively. The enhancement of SC

upon Ni is rather rare, which is only observed in iron-based superconductors (Sefat et al., 2008; Ni et al., 2010). Furthermore, in terms of crystal structure, this enhancement is related to squeezing the $[Cu_5As_3]^{2-}$ along the c-axis as $x < 0.4$, and the suppression of T_c corresponds to a contraction of $[Cu_5As_3]^{2-}$ along the a-axis, as shown in the inset of Figure 5A. The phase diagram is similar to those of cuprates and iron-based superconductors to a large extent, which features the competition of structural distortion and SC.

DISCUSSION

We calculated the electronic structure in the paramagnetic state from density functional theory calculations. The band structures of La2532 are shown in Figure 5B, where a small hole-pocket and three large electron-pockets show up at the Γ and M points, respectively. Around E_F, the bands along the Γ-X and Γ-Y directions have large dispersion, whereas the bands along Γ-Z are almost flat, indicating that the Fermi surfaces are quasi-two-dimensional. The hole-pocket is mainly composed of Cu(1) $d_{x^2-y^2}$ hybridizing with As(1) P_z, and the electron-pocket components are Cu(1) d_{xz}/d_{yz}, d_{xy}, and As(1) $P_{x/y}$ (Figure S12). It is noted that the Cu(1) d_{xz}/d_{yz} dominates the states at Fermi energy (E_F), different from that in cuprate superconductors (Uchida, 2015). In Figure 5C, one clearly sees that the E_F is dominated by Cu(1) d and As(1) p states. There are higher $N(E_F)$ at −0.1 eV below E_F; therefore doping Ni with one electron less can lower the E_F, which is theoretically reasonable to induce higher $N(E_F)$ and T_c. The total $N(E_F)$ is 1.75 states/eV formula unit (f. u.), and the estimated bare Sommerfeld coefficient is 2.06 mJ mol^{-1} K^{-2}. According to the equation $\gamma_n = \gamma_b(1+\lambda_{e-p}) (1+\lambda_{e-e})$, if we assume the electron-electron coupling $\lambda_{e-e} = 0$, one would can obtain an electron-phonon coupling $\lambda_{e-p} = 1.43$. The large λ_{e-p} exceeds the limit of BCS framework, implying that the electron-electron coupling cannot be ignored.

It has been previously reported that the bonded anionic dimer can induce ferromagnetic critical point, SC, and metal-insulator transition (Jia et al., 2011; Guo et al., 2012; Radaelli et al., 2002). Here, there are weak bonding states of As(1)-As(2) in $RE_2Cu_5As_3O_2$, and the E_F will be higher than the bonding orbital (σ) and locates the bottom of the anti-bonding orbital (σ^*) (Hoffmann and Zheng, 1985; Hoffmann, 1988). As $x < 0.4$, the doped holes would first enter into the As(1)-As(2) bond and lift the valence of As^{3-}. The strengthened bond between apical As(1)-central As(2) rapidly shortens the c-axis. At the same time, the E_F slowly drops to the energy between σ and σ^* orbital. As $x > 0.4$, the shrinking of As(1)-As(2) bond length and c-axis slows, and then the a-axis begins to quickly decrease. It means that some excess holes are introduced into the lattice, which possibly suppresses the SC. The Hall measurement, shown in Figure S13, shows positive Hall coefficients. It indicates that the dominant carriers are holes. Using the single-band model, we obtain a carrier concentration of $\sim10^{22}$ cm^{-3}, which is slightly increased in 40% Ni-doped La2532.

Still, the static magnetic order associated with Cu ions is not observed in all samples measured above 1.8 K, and all the $\chi(T)$ curves can be fitted by Curie-Weiss equation; see Figure S14. The $4f^0$ La2532 is an itinerant compound with AFM interaction ($\mu_{eff} = 0.16\mu_B$ per Cu; $\theta = -148$ K). For 40% and 100% Ni-doped La2532, the resultant μ_{eff} and θ are 0.56 μ_B/Cu and −256 K and 0.69 μ_B/Cu and −424 K, respectively. It means that the Ni-doped samples have larger μ_{eff} and stronger AFM interaction. However, these moments are still much smaller than the theoretical value (1.73 μ_B) for Cu^{2+} ions with $S = 1/2$. It means that the magnetic interaction is not fully localized and the emergence of Cu-Cu metallic bonds in $[Cu_5As_3]^{2-}$ significantly increases the amount of itinerant electrons. The SC here is likely to be an itinerant picture (Singh and Du, 2008; Dong et al., 2008), which is similar to those of BaNi$_2$As$_2$ and LaNiAsO (Subedi and Singh, 2008; Boeri et al., 2009). In Pr2532 and Nd2532, the total μ_{eff} and θ are 4.42 μ_B/Pr and −26.5 K and 4.62 μ_B/Nd and −30.4 K, respectively. The μ_{eff} is larger than the values for the magnetic Pr^{3+} ($4f^2$, 3.58 μ_B) and Nd^{3+} ($4f^3$, 3.62 μ_B) in Ni-based superconductors (Li et al., 2014), indicating that the magnetic contribution of Cu ions is important. As the carrier doping can suppress the moment of RE^{3+} (Zhao et al., 2008), we cannot summarize clear variation of magnetic moment of Cu ions in Ni-doped Pr2532 and Nd2532. High-precision experiments are called for to identify Cu's magnetism.

The results provide a novel kind of Cu-based superconductor $RE_2Cu_5As_3O_2$ (RE = La, Pr, Nd), whose crystal structure, SC, and ground states can be effectively tuned through a rather wide range of Ni doping. The dome-like T_c in turn is induced by the dimerization of As-As bonds along the c-axis and shrinking of a-axis. The robust SC against Ni, structural anomaly, and enhanced AFM interaction provide new perspectives to understand the superconducting mechanism.

METHODS

All methods can be found in the accompanying Transparent Methods supplemental file.

SUPPLEMENTAL INFORMATION

Supplemental Information can be found online at https://doi.org/10.1016/j.isci.2019.03.026.

AUTHOR CONTRIBUTIONS

J.G. and X.L.C. provided strategy and advice for the material exploration. X.C., J.G., and C.G. performed the sample fabrication, measurements, and fundamental data analysis. E.C., T.Y., and S.L. measured the low-temperature properties. C.L., N.L., and J.H. carried out the theoretical calculation. Q.Z. measured the HAADF images. J.G. X.C and X.L.C. wrote the manuscript based on discussion with all the authors.

DECLARATION OF INTERESTS

The authors declare no competing interests.

REFERENCES

Boeri, L., Dolgov, O.V., and Golubov, A.A. (2009). Electron-phonon properties of pnictide superconductors. Phys. C 469, 628–634.

Canfield, P.C., Bud'ko, S.L., Ni, N., Yan, J.Q., and Kracher, A. (2009). Decoupling of the superconducting and magnetic/structural phase transitions in electron-doped $BaFe_2As_2$. Phys. Rev. B 80, 060501(R).

Chen, X.L., Liang, J.K., Xie, S.S., Qiao, Z.Y., Tong, X.S., and Xing, X.R. (1992). Superconductivity and magnetic properties in $Pr_{0.2}Yb_{0.8-x}La_xBa_2Cu_3O_{7-\delta}$. Z. Phys. 88, 1–4.

Chen, X.L., Liang, J.K., Wang, Y., Wu, F., and Rao, G.H. (1995). Superconductivity in $Y_{0.6}Pr_{0.4}Ba_{2-x}Sr_xCu_3O_{7-\delta}$: the role of apical oxygen in hybridization. Phys. Rev. B 51, 16444–16447.

Dai, P.C., Hu, J.P., and Dagotto, E. (2012). Magnetism and its microscopic origin in iron-based high-temperature superconductors. Nat. Phys. 8, 709–718.

Dong, J., Zhang, H.J., Xu, G., Li, Z., Li, G., Hu, W.Z., Wu, D., Chen, G.F., Dai, X., Luo, J.L., et al. (2008). Competing orders and spin-density-wave instability in $La(O_{1-x}F_x)FeAs$. Europhys. Lett. 83, 27006.

Dünner, J., and Mewis, A. (1995). $BaCu_6P_2$ and $BaCu_6As_2$ - two compounds with a periodic intergrowth of $ThCr_2Si_2$ and Cu structure-type segments. J. Alloys Compd. 221, 65–69.

Guo, J.G., Qi, Y.P., Matsuishi, S., and Hosono, H. (2012). T_c Maximum in solid solution of Pyrite $IrSe_2$–$RhSe_2$ induced by destabilization of anion dimers. J. Am. Chem. Soc. 134, 20001–20004.

Hoffmann, R. (1988). Solids and Surfaces: A Chemist's View of Bonding in Extended Structures (VCH).

Hoffmann, R., and Zheng, C. (1985). Making and breaking bonds in the solid state: the thorium chromium silicide ($ThCr_2Si_2$) structure. J. Phys. Chem. 89, 4175–4181.

Huang, Q., Qiu, Y., Bao, W., Green, M.A., Lynn, J.W., Gasparovic, Y.C., Wu, T., Wu, G., and Chen, X.H. (2008). Neutron-diffraction measurements of magnetic order and a structural transition in the parent $BaFe_2As_2$ compound of FeAs-Based high-temperature superconductors. Phys. Rev. Lett. 101, 257003.

Ideta, S., Yoshida, T., Nishi, I., Fujimori, A., Kotani, Y., Ono, K., Nakashima, Y., Yamaichi, S., Sasagawa, T., Nakajima, M., et al. (2011). Fermi-surface evolution by transition-metal substitution in the iron-based superconductor LaFeAsO. J. Phys. Soc. Jpn. 80, 123701.

Ideta, S., Yoshida, T., Nishi, I., Fujimori, A., Kotani, Y., Ono, K., Nakashima, Y., Yamaichi, S., Sasagawa, T., Nakajima, M., et al. (2013). Dependence of carrier doping on the impurity potential in transition-metal-substituted FeAs-based superconductors. Phys. Rev. Lett. 110, 107007.

Jia, S., Jiramongkolchai, P., Suchomel, M.R., Toby, B.H., Checkelsky, J.G., Ong, N.P., and Cava, R.J. (2011). Ferromagnetic quantum critical point induced by dimer-breaking in $SrCo_2(Ge_{1-x}P_x)_2$. Nat. Phys. 7, 207–210.

Kamihara, Y., Watanabe, T., Hirano, M., and Hosono, H. (2008). Iron-based layered superconductor $La[O_{1-x}F_x]FeAs$ (x=0.05–0.12) with T_c=26 K. J. Am. Chem. Soc. 130, 3296–3297.

Kuroki, K., Onari, S., Arita, R., Usui, H., Tanaka, Y., Kontani, H., and Aoki, H. (2008). Unconventional pairing originating from the disconnected Fermi surfaces of superconducting $LaFeAsO_{1-x}F_x$. Phys. Rev. Lett. 101, 087004.

Lee, P.A., Nagaosa, N., and Wen, X.G. (2006). Doping a Mott insulator: physics of high-temperature superconductivity. Rev. Mod. Phys. 78, 17–85.

Li, L.J., Luo, Y.K., Wang, Q.B., Chen, H., Ren, Z., Tao, Q., Li, Y.K., Lin, X., He, M., Zhu, Z.W., et al. (2009). Superconductivity induced by Ni doping in $BaFe_2As_2$ single crystals. New J. Phys. 11, 025008.

Li, Y.K., Luo, Y.K., Li, L., Chen, B., Xu, X.F., Dai, J.H., Yang, X.J., Zhang, L., Cao, G.H., and Xu, Z.A. (2014). Kramers non-magnetic superconductivity in LnNiAsO superconductors. J. Phys. Condens. Matter 26, 425701.

Mazin, I.I. (2010). Superconductivity gets an iron boost. Nature 464, 183.

Mazin, I.I., Singh, D.J., Johannes, M.D., and Du, M.H. (2008). Unconventional superconductivity with a sign reversal in the order parameter of $LaFeAsO_{1-x}F_x$. Phys. Rev. Lett. *101*, 057003.

Mu, G., Wang, Y., Shan, L., and Wen, H.H. (2007). Possible nodeless superconductivity in the noncentrosymmetric superconductor $Mg_{12-\delta}Ir_{19}B_{16}$. Phys. Rev. B *76*, 064527.

Nakajima, M., Ishida, S., Tanaka, T., Kihou, K., Tomioka, Y., Saito, T., Lee, C.H., Fukazawa, H., Kohori, Y., Kakeshita, T., et al. (2014). Strong electronic correlations in iron pnictides: comparison of optical spectra for $BaFe_2As_2$-related compounds. J. Phys. Soc. Jpn. *83*, 104703.

Neilson, J.R., McQueen, T.M., Llobet, A., Wen, J., and Suchomel, M.R. (2013). Charge density wave fluctuations, heavy electrons, and superconductivity in KNi_2S_2. Phys. Rev. B *87*, 045124.

Ni, N., Thaler, A., Yan, J.Q., Kracher, A., Colombier, E., Bud'ko, S.L., Canfield, P.C., and Hannahs, S.T. (2010). Temperature versus doping phase diagrams for $Ba(Fe_{1-x}TM_x)_2As_2$ (TM=Ni, Cu, Cu/Co) single crystals. Phys. Rev. B *82*, 024519.

Onari, S., and Kontani, H. (2009). Violation of Anderson's theorem for the sign-reversing *s*-wave state of iron-pnictide superconductors. Phys. Rev. Lett. *103*, 177001.

Popovich, P., Boris, A.V., Dolgov, O.V., Golubov, A.A., Sun, D.L., Lin, C.T., Kremer, R.K., and Keimer, B. (2010). Specific heat measurements of $Ba_{0.68}K_{0.32}Fe_2As_2$ single crystals: evidence for a multiband strong-coupling superconducting state. Phys. Rev. Lett. *105*, 027003.

Radaelli, P.G., Horibe, Y., Gutmann, M.J., Ishibashi, H., Chen, C.H., Ibberson, R.M., Koyama, Y., Hor, Y.S., Kiryukhin, V., and Cheong, S.W. (2002). Formation of isomorphic Ir^{3+} and Ir^{4+} octamers and spin dimerization in the spinel $CuIr_2S_4$. Nature *416*, 155–158.

Rotter, M., Tegel, M., and Johrendt, D. (2008). Superconductivity at 38 K in the iron arsenide $(Ba_{1-x}K_x)Fe_2As_2$. Phys. Rev. Lett. *101*, 107006.

Saparov, B., and Sefat, A.S. (2012). Metallic properties of $Ba_2Cu_3P_4$ and $BaCu_2Pn_2$ (Pn=As, Sb). J. Solid State Chem. *191*, 213–219.

Sefat, A.S., Jin, R., McGuire, M.A., Sales, B.C., Singh, D.J., and Mandrus, D. (2008). Superconductivity at 22 K in Co-doped $BaFe_2As_2$ crystals. Phys. Rev. Lett. *101*, 117004.

Singh, D.J., and Du, M.H. (2008). Density functional study of LaFeAsO1-xFx: a Low carrier density superconductor near itinerant magnetism. Phys. Rev. Lett. *100*, 237003.

Subedi, A., and Singh, D.J. (2008). Density functional study of $BaNi_2As_2$: electronic structure, phonons, and electron-phonon superconductivity. Phys. Rev. B *78*, 132511.

Tsuei, C.C., and Kirtley, J.R. (2000). Pairing symmetry in cuprate superconductors. Rev. Mod. Phys. *72*, 969–1016.

Uchida, S. (2015). High Temperature Superconductivity: The Road to Higher Critical Temperature (Springer Verlag).

Wollman, D.A., Vanharlingen, D.J., Lee, W.C., Ginsberg, D.M., and Leggett, A.J. (1993). Experimental determination of the superconducting pairing state in YBCO from the phase coherence of YBCO-Pb dc SQUIDs. Phys. Rev. Lett. *71*, 2134–2137.

Xiao, G., Cieplak, M.Z., Xiao, J.Q., and Chien, C.L. (1990). Magnetic pair-breaking effects: moment formation and critical doping level in superconducting $La_{1.85}Sr_{0.15}Cu_{1-x}A_xO_4$ systems (A=Fe, Co, Ni, Zn, Ga, Al). Phys. Rev. B *42*, 8752–8755.

Yakita, H., Ogino, H., Okada, T., Yamamoto, A., Kishio, K., Tohei, T., Ikuhara, Y., Gotoh, Y., Fujihisa, H., Kataoka, K., et al. (2014). A new layered iron arsenide superconductor: (Ca,Pr) $FeAs_2$. J. Am. Chem. Soc. *136*, 846–849.

Zhao, J., Huang, Q., de La Cruz, C., Li, S.L., Lynn, J.W., Chen, Y., Green, M.A., Chen, G.F., Li, G., Li, Z., et al. (2008). Structural and magnetic phase diagram of $CeFeAsO_{1-x}F_x$ and its relation to high-temperature superconductivity. Nat. Mater. *7*, 953–959.

Supplemental Information

Anomalous Dome-like Superconductivity

in RE$_2$(Cu$_{1-x}$Ni$_x$)$_5$As$_3$O$_2$ (RE = La, Pr, Nd)

Xu Chen, Jiangang Guo, Chunsheng Gong, Erjian Cheng, Congcong Le, Ning Liu, Tianping Ying, Qinghua Zhang, Jiangping Hu, Shiyan Li, and Xiaolong Chen

Supplemental Information

Table S1. Summary of selected crystallographic parameters of $RE_2(Cu_{1-x}Ni_x)_5As_3O_2$ (RE=La, Pr, Nd) (space group $I4/mmm$, $Z=2$) taken form the Rietveld refinements results. The sites of Cu(2) (0, 0, 0.5), O(1) (0.5, 0, 0.25), As(2) (0, 0, 0) are fixed. Related to Figure 1 and Figure 3.

RE=La	$x=0$	$x=0.06$	$x=0.1$	$x=0.2$	$x=0.3$	$x=0.35$	$x=0.4$
a (Å)	4.1386 (1)	4.1422 (1)	4.1422 (1)	4.1439 (1)	4.1436 (1)	4.1426 (1)	4.1427 (1)
c (Å)	22.8678 (6)	22.7929 (5)	22.7046 (8)	22.6210 (9)	22.5215 (6)	22.4479 (6)	22.4418 (8)
V (Å^3)	391.66 (1)	391.07(1)	390.38 (2)	388.45 (2)	386.68 (2)	385.24 (2)	385.14 (2)
R_p	2.95	3.02	3.14	3.80	2.38	2.67	3.58
R_{wp}	4.26	4.66	4.83	5.38	3.55	3.87	4.91
R_{expt}	2.17	1.81	1.87	3.11	1.87	1.68	3.22
χ^2	3.87	6.64	6.69	2.99	3.60	5.27	2.32
Atomic sites							
La(1) (0.5, 0.5, z1)	0.1975 (1)	0.1983 (1)	0.1982 (1)	0.1978 (1)	0.1980 (1)	0.1978 (1)	0.1980 (1)
Cu(1) (0.5, 0, z2)	0.0689 (1)	0.0690 (1)	0.0685 (1)	0.0691 (1)	0.0684 (1)	0.0680 (1)	0.0684 (1)
As(1) (0, 0, z3)	0.1229 (1)	0.1223 (1)	0.1213 (2)	0.1208 (1)	0.1196 (1)	0.1194 (1)	0.1200 (1)
As(1)-As(2)	2.810 (1)	2.782 (1)	2.763 (1)	2.732 (1)	2.694 (1)	2.681 (1)	2.687 (1)
Cu(1)-Cu(2)	2.600 (1)	2.599 (2)	2.592 (2)	2.595 (2)	2.581 (2)	2.572 (1)	2.578 (2)

RE=La	$x=0.45$	$x=0.5$	$x=0.6$	$x=0.7$	$x=0.8$	$x=0.9$	$x=1.0$
a (Å)	4.1364 (1)	4.1307 (1)	4.1226 (2)	4.1066 (1)	4.0943 (1)	4.0797 (1)	4.0686 (1)
c (Å)	22.4300 (6)	22.4330 (6)	22.4420 (1)	22.4451 (7)	22.4622 (6)	22.4789 (4)	22.4775 (3)
V (Å^3)	383.77 (1)	382.76 (1)	381.43 (3)	378.51 (2)	376.54 (1)	374.13 (1)	372.08 (1)
R_p	2.60	2.35	3.80	2.40	3.60	2.34	2.53
R_{wp}	4.05	3.45	5.26	3.57	4.80	3.45	3.87
R_{expt}	1.75	1.77	3.07	1.75	3.03	1.80	1.65
χ^2	5.33	3.81	2.93	4.15	2.51	3.69	5.50
Atomic sites							
La(1) (0.5, 0.5, z1)	0.1981 (1)	0.1981 (1)	0.1977 (1)	0.1971 (1)	0.1963 (1)	0.1966 (1)	0.1956 (1)
Cu(1) (0.5, 0, z2)	0.0683 (1)	0.0682 (1)	0.0663 (2)	0.0657 (1)	0.0636 (1)	0.0648 (1)	0.0648 (1)
As(1) (0, 0, z3)	0.1195 (1)	0.1199 (1)	0.1184 (2)	0.1184 (1)	0.1175 (1)	0.1169 (1)	0.1171 (1)
As(1)-As(2)	2.681 (1)	2.680 (1)	2.656 (1)	2.657 (1)	2.639 (1)	2.630 (1)	2.630 (1)
Cu(1)-Cu(2)	2.574 (2)	2.570 (1)	2.542 (3)	2.528 (2)	2.496 (3)	2.507 (2)	2.502 (2)

RE=Pr	x=0.0	x=0.3	x=0.35	x=0.4	x=0.45	x=0.5	x=0.9	x=1.0
a (Å)	4.0802 (1)	4.0974 (1)	4.0983 (1)	4.0954 (2)	4.0912 (1)	4.0879 (1)	4.0326 (1)	4.0213 (1)
c (Å)	22.9144 (5)	22.3197 (8)	22.2761 (9)	22.2673 (9)	22.2673 (8)	22.2702 (7)	22.3416 (6)	22.3555 (6)
V (Å³)	381.49 (1)	374.73 (2)	374.16 (2)	373.47 (3)	372.71 (2)	372.15 (2)	363.31 (1)	361.50 (1)
R_p	2.88	2.55	2.50	3.30	2.56	2.21	2.39	2.47
R_{wp}	4.29	3.82	3.61	5.98	3.86	3.24	3.51	3.77
R_{expt}	1.82	1.72	1.78	1.72	1.75	1.76	1.72	1.76
χ^2	5.54	4.94	4.09	12.1	4.85	3.38	4.15	4.61
Atomic sites								
Pr(1) (0.5, 0.5, z1)	0.1995 (1)	0.1993 (1)	0.1985 (1)	0.1989 (1)	0.1985 (1)	0.1985 (1)	0.1974 (1)	0.1972 (1)
Cu(1) (0.5, 0, z2)	0.0711 (1)	0.0693 (1)	0.0691 (1)	0.0700 (2)	0.0690 (1)	0.0687 (1)	0.0661 (1)	0.0660 (2)
As(1) (0, 0, z3)	0.1275 (1)	0.1233 (1)	0.1223 (1)	0.1224 (2)	0.1230 (1)	0.1222 (1)	0.1199 (1)	0.1199 (1)
As(1)-As(2)	2.920 (3)	2.753 (3)	2.724 (3)	2.726 (5)	2.739 (3)	2.720 (3)	2.678 (3)	2.680 (4)
Cu(1)-Cu(2)	2.611 (2)	2.567 (2)	2.563 (2)	2.573 (3)	2.558 (2)	2.554 (2)	2.500 (2)	2.494 (2)

RE=Nd	x=0.0	x=0.3	x=0.35	x=0.4	x=0.45	x=0.5	x=0.9	x=1.0
a (Å)	4.0561 (1)	4.0777 (1)	4.0807 (1)	4.0813 (1)	4.0776 (1)	4.0720 (1)	4.0145 (1)	4.0039 (1)
c (Å)	23.0082 (6)	22.3833 (7)	22.2845 (8)	22.2574 (7)	22.2446 (9)	22.2509 (8)	22.3335 (6)	22.3439 (5)
V (Å³)	378352 (2)	372.19 (2)	371.07 (2)	370.75 (2)	369.86 (2)	368.95 (1)	359.93 (2)	358.19 (1)
R_p	2.70	2.52	2.35	2.60	2.31	2.15	2.73	2.37
R_{wp}	3.88	3.63	3.47	3.71	3.43	3.07	4.24	3.32
R_{expt}	2.07	1.78	1.82	1.97	1.68	1.74	1.75	1.76
χ^2	3.50	4.16	3.65	3.57	4.18	3.13	5.83	3.57
Atomic sites								
Nd(1) (0.5, 0.5, z1)	0.1998 (1)	0.1993 (1)	0.1993 (1)	0.1987 (1)	0.1990 (1)	0.1987 (1)	0.1979 (1)	0.1977 (1)
Cu(1) (0.5, 0, z2)	0.0717 (2)	0.0702 (1)	0.0705 (1)	0.0701 (1)	0.0698 (1)	0.0692 (1)	0.0664 (2)	0.0654 (1)
As(1) (0, 0, z3)	0.1286 (2)	0.1241 (1)	0.1235 (1)	0.1236 (1)	0.1238 (1)	0.1233 (1)	0.1210 (2)	0.1209 (1)
As(1)-As(2)	2.9590 (5)	2.778 (3)	2.753 (3)	2.750 (3)	2.753 (3)	2.743 (3)	2.701 (4)	2.701 (3)
Cu(1)-Cu(2)	2.641 (3)	2.575 (2)	2.575 (2)	2.568 (2)	2.562 (2)	2.553 (1)	2.495 (3)	2.479 (2)

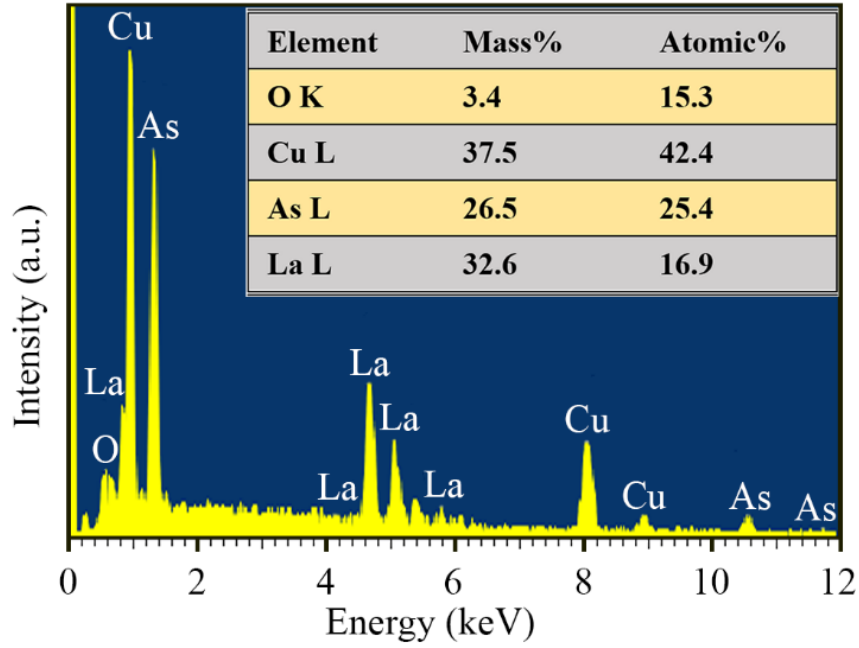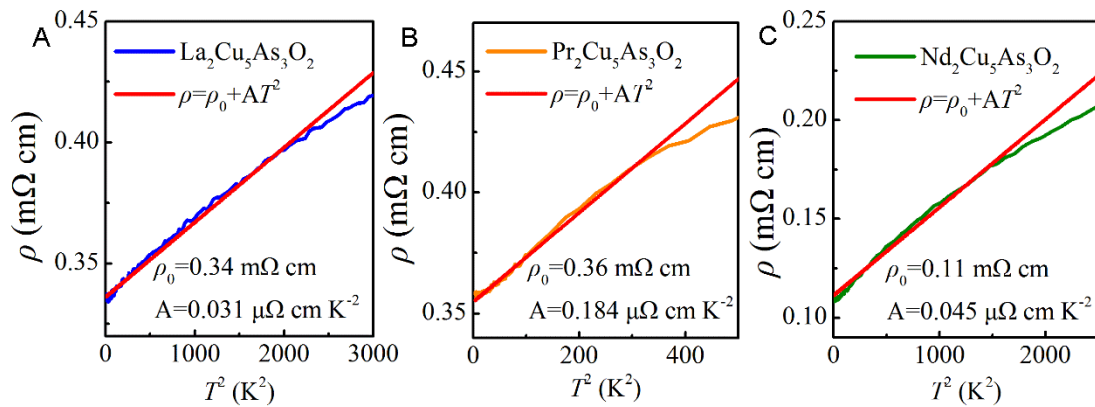**Figure S1. Energy dispersive spectroscopy (EDS) of La$_2$Cu$_5$As$_3$O$_2$.** Related to Figure 1.

Figure S2. Electrical resistivity below transition can be fitted by $\rho=\rho_0+AT^2$, suggesting typical Fermi-liquid behavior in La$_2$Cu$_5$As$_3$O$_2$ (A), Pr$_2$Cu$_5$As$_3$O$_2$ (B) and Nd$_2$Cu$_5$As$_3$O$_2$ (C). Fitting interval segment is close to the T^*, which might lead to large value of A coefficient. Related to Figure 2.
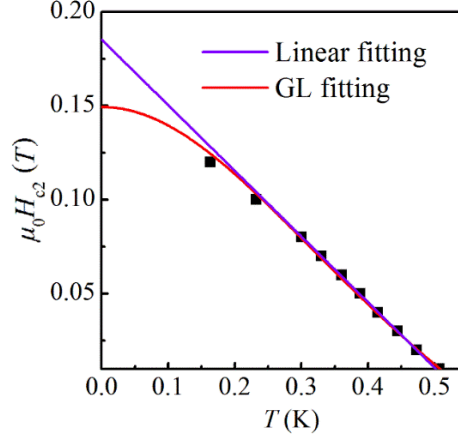
Figure S3. Upper critical field, $\mu_0H_{c2}(0)$, of La$_2$Cu$_5$As$_3$O$_2$ estimated from linear and Ginzburg-Landau fitting. Related to Figure 2.
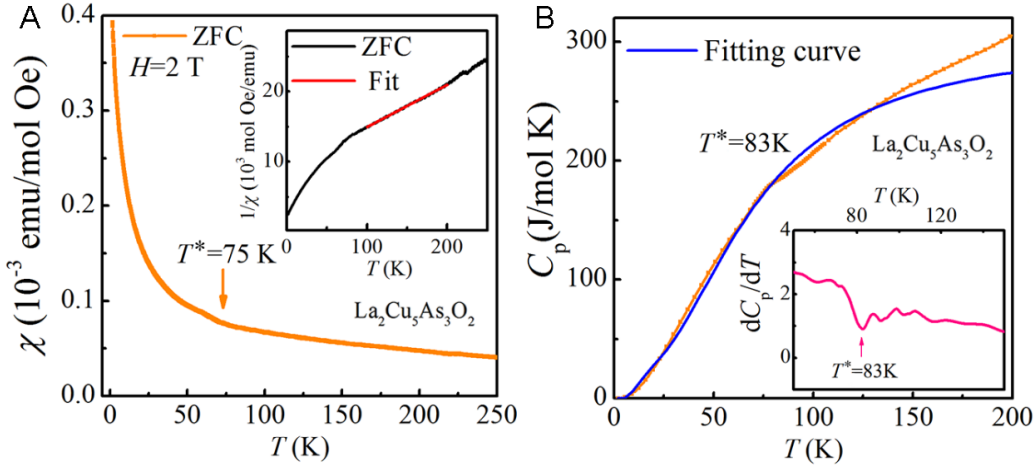
Figure S4. The physical properties of La$_2$Cu$_5$As$_3$O$_2$. (A) Temperature-dependent magnetic susceptibility (χ) measured at 2 T field. The inset shows the inverse χ and the data fitting from 100 K-200 K by Curie-Weiss equation, $1/\chi=(T-\theta)/C$. θ is Curie temperature and C is Curie constant. The magnetic susceptibility (χ) of La$_2$Cu$_5$As$_3$O$_2$ at normal state increases with temperature decreasing, and there is also a small kink at ~75 K. The inset is the temperature dependent inverse susceptibility that can be well fitted by Curie-Weiss equation from 100 K to 200 K. The estimated magnetic moment is ~0.16 μ_B and θ=-148(1) K. (B) Heat capacity (C_p) as a function of temperature, and a transition can be observed at T^*=83 K as the inset of derivation of C_p. The solid blue line is the fitting curve from the sum of electronic and phonon contributions,

$$C_p = \gamma T + C_D \; ; \quad C_D = 9N_d R(\frac{T}{\Theta_D})^3 \int_0^{\Theta_D/T} \frac{\zeta^4 e^\zeta}{(e^\zeta - 1)^2} d\zeta$$

where C_D is the contributions of phonon. N_d is 12. R is the gas constant. Θ_D is Debye temperature. The converged fitting gave Debye temperature Θ_D is 169(2) K and Sommerfeld coefficient γ_0 is 5.01 mJ·mol^{-1}·K^{-2}. The C_p over the theoretical value above 150 K may be on account of boundaries scattering in polycrystalline pellets. Related to Figure 2.
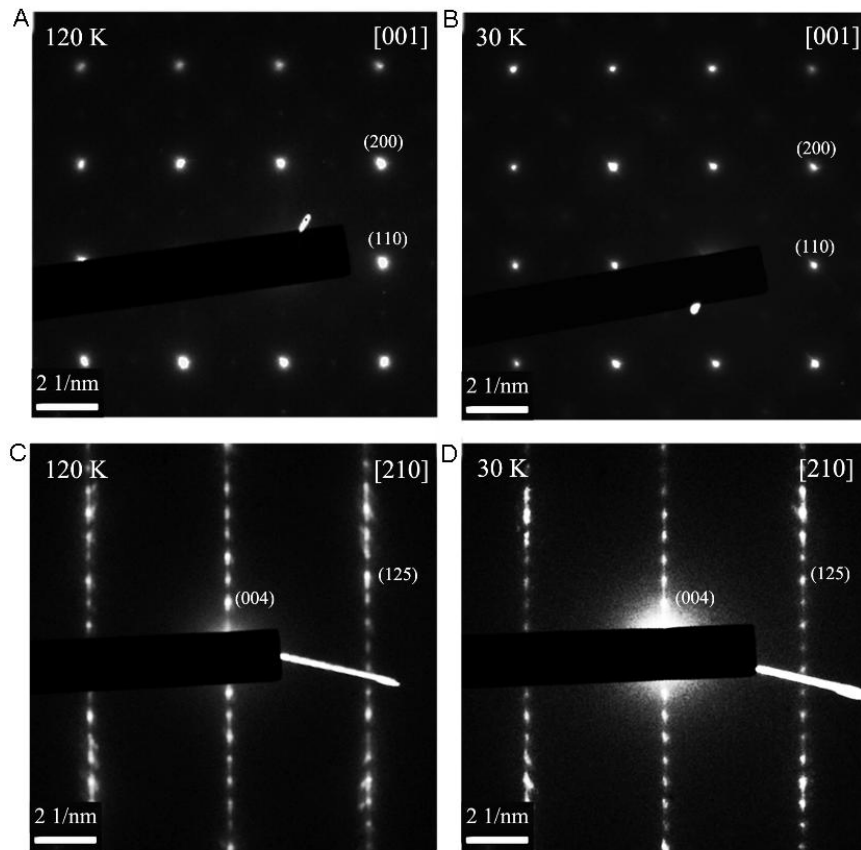
Figure S5. Transmission electron microscopy images of La$_2$Cu$_5$As$_3$O$_2$ taken at 120 K and 30 K along [001] (A, B) and [210] zone axes (C, D). No any satellite spots can be observed under 30 K, which excludes the existence of charge density wave transition. Related to Figure 2.
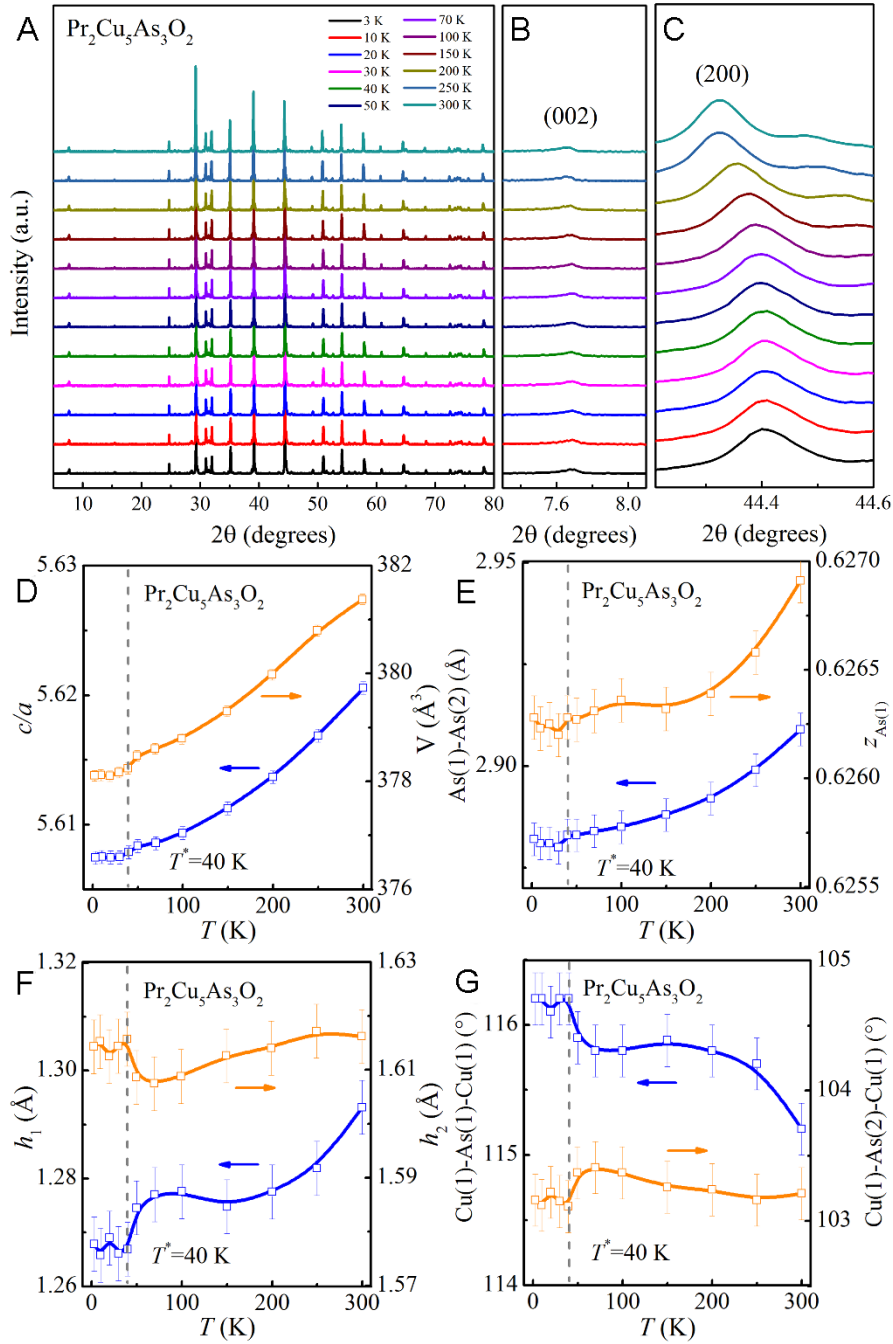
Figure S6. Powder X-ray diffraction patterns and crystallographic parameters of Pr₂Cu₅As₃O₂ at various temperatures. (A-C) Temperature-dependent PXRD pattern, (002) and (200) peaks. (D-G) Crystallographic parameters of c/a ratio, As(1)-As(2) bond length, $z_{As(1)}$, h_1, h_2, Cu(1)-As(1)-Cu(1) angle and Cu(1)-As(2)-Cu(1) angle versus temperature. Related to Figure 2.
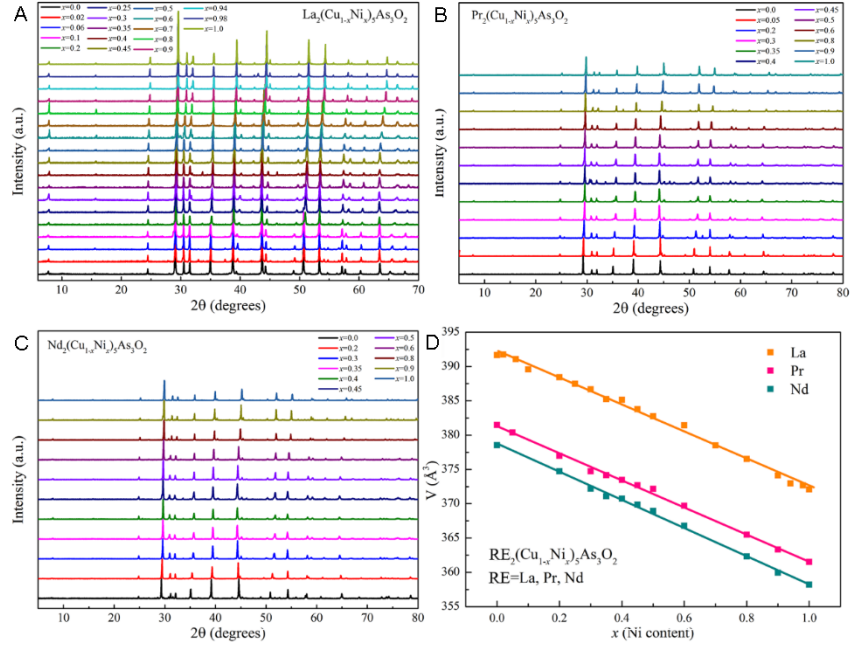
Figure S7. Powder X-ray diffraction patterns and volume variation of RE$_2$(Cu$_{1-x}$Ni$_x$)$_5$As$_3$O$_2$ as a function of Ni content. (A, B, C) PXRD patterns of RE$_2$(Cu$_{1-x}$Ni$_x$)$_5$As$_3$O$_2$ (x=0-1.0, RE=La, Pr, Nd). All peaks systemically shifts upon Ni doping, indicating continuous solid solutions. Tiny La$_2$O$_3$ and NiAs impurity can be observed. (D) Ni-dependent of volume of unit cell for RE$_2$(Cu$_{1-x}$Ni$_x$)$_5$As$_3$O$_2$. The linear decreasing indicates that the Ni has been successfully doped into RE$_2$Cu$_5$As$_3$O$_2$. Related to Figure 3.
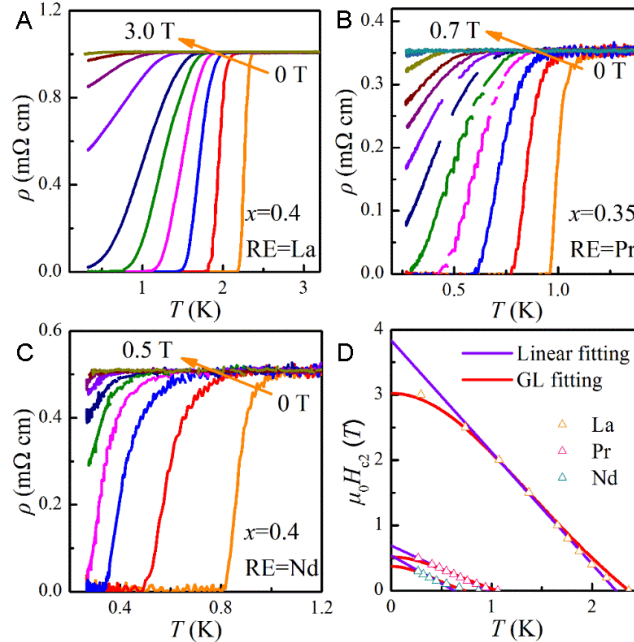
Figure S8. Superconducting transition against external magnetic fields of RE$_2$(Cu$_{1-x}$Ni$_x$)$_5$As$_3$O$_2$ (x~0.4). (A, B, C) Electrical resistivity of La$_2$(Cu$_{0.6}$Ni$_{0.4}$)$_5$As$_3$O$_2$, Pr$_2$(Cu$_{0.65}$Ni$_{0.35}$)$_5$As$_3$O$_2$ and Nd$_2$(Cu$_{0.6}$Ni$_{0.4}$)$_5$As$_3$O$_2$ under different magnetic fields. (D) Upper μ_0H_{c2}(0) of three samples are estimated from linear and GL fitting of 10% normal-state resistivity. Related to Figure 4.
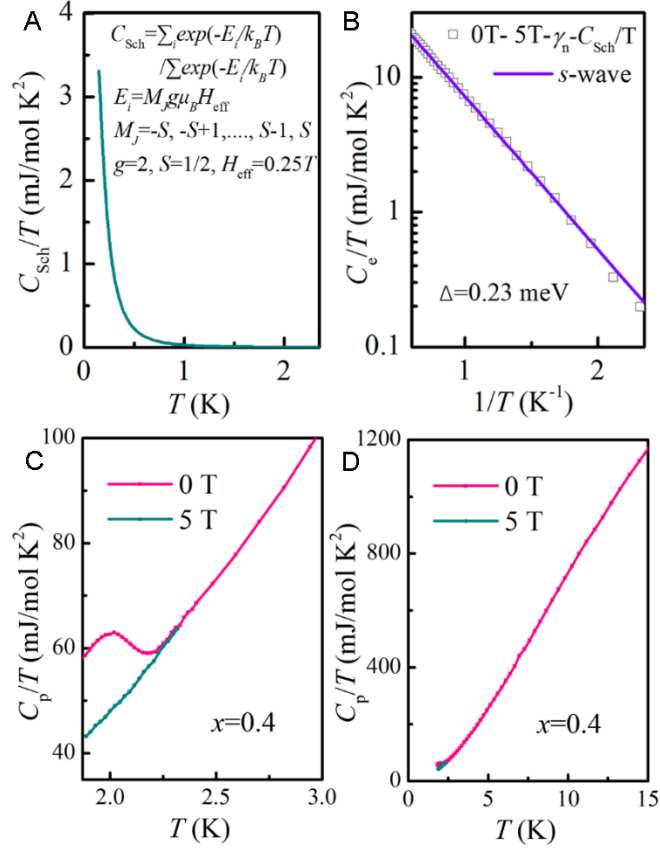
Figure S9. Heat capacity of La$_2$(Cu$_{0.6}$Ni$_{0.4}$)$_5$As$_3$O$_2$. (A) Detail of estimating Schottky term of C_{Sch}/T using the inset parameters. (B) Semi-logarithmic of C_e/T of La$_2$(Cu$_{0.6}$Ni$_{0.4}$)$_5$As$_3$O$_2$ as a function of temperature. (C, D) C_p/T of La$_2$(Cu$_{0.6}$Ni$_{0.4}$)$_5$As$_3$O$_2$ at wide temperature range from 1.8 K to 3 K and 1.8 K to 15 K. Related to Figure 4.
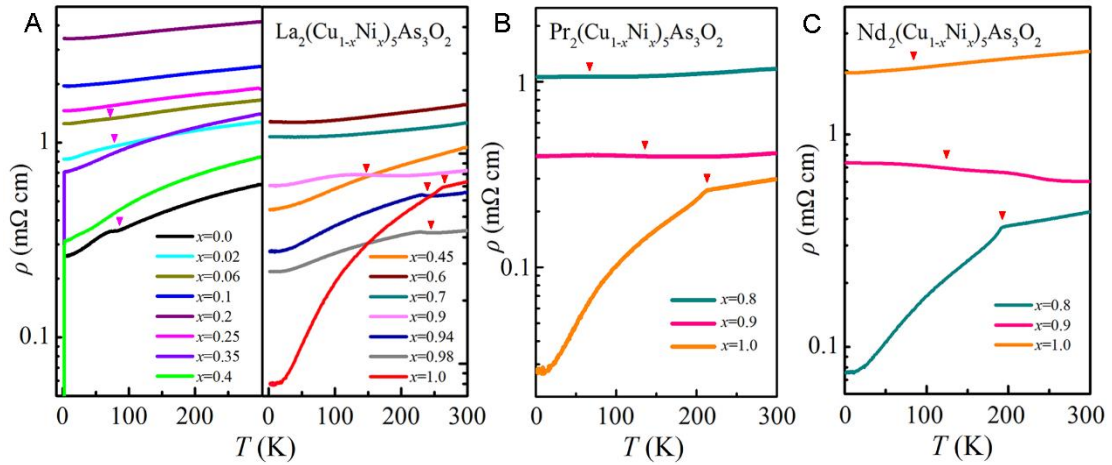
Figure S10. Transport properties of RE$_2$(Cu$_{1-x}$Ni$_x$)$_5$As$_3$O$_2$. (A) Electrical resistivity of La$_2$(Cu$_{1-x}$Ni$_x$)$_5$As$_3$O$_2$ (x=0-1.0) from 1.8 K-300 K. (B) Electrical resistivity of Ni-doped Pr$_2$(Cu$_{1-x}$Ni$_x$)$_5$As$_3$O$_2$ (x=0.8, 0.9, 1.0) from 1.8 K-300 K. (C) Electrical resistivity of Ni-doped Nd$_2$(Cu$_{1-x}$Ni$_x$)$_5$As$_3$O$_2$ (x=0.8, 0.9, 1.0) from 1.8 K-300 K. The arrows represent the resistivity anomaly of undetermined transition (x<0.1) or structure phase transition (x>0.8). Related to Figure 5.
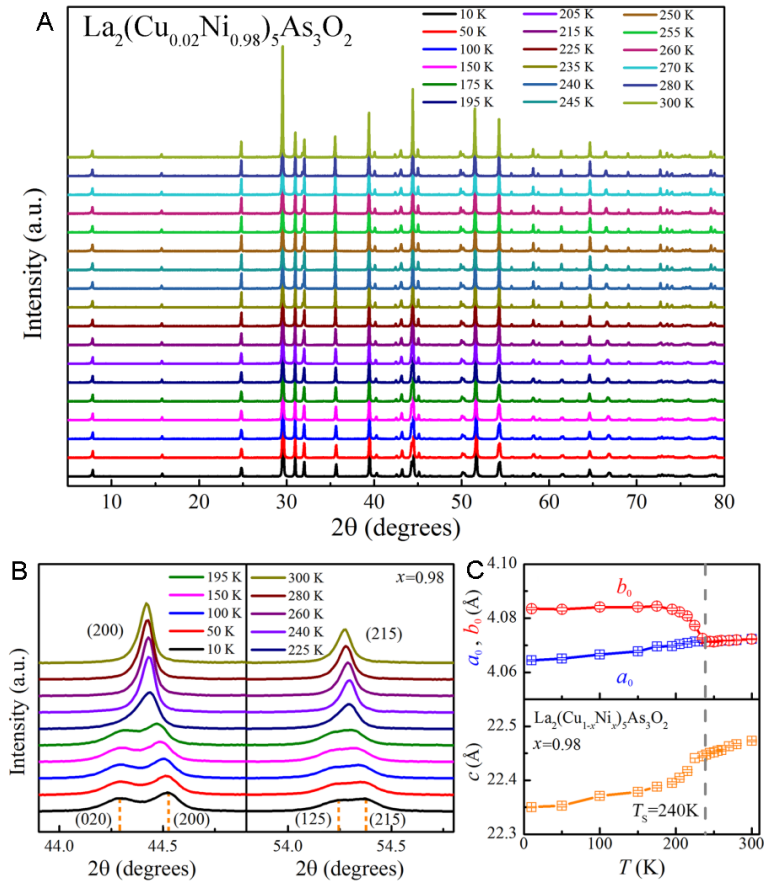
Figure S11. Powder X-ray diffraction patterns and crystallographic parameters of La$_2$(Cu$_{0.02}$Ni$_{0.98}$)$_5$As$_3$O$_2$ at various temperatures. (A) PXRD patterns of La$_2$(Cu$_{0.02}$Ni$_{0.98}$)$_5$As$_3$O$_2$ from 10 K to 300 K. (B) Splitting of (200) and (215) peaks of x=0.98 from 10 K-300 K. (C) Temperature-dependent lattice constants of La$_2$(Cu$_{0.02}$Ni$_{0.98}$)$_5$As$_3$O$_2$. Below 240 K, there is orthorhombic phase transition with splitting of a-lattice parameters. Related to Figure 5.
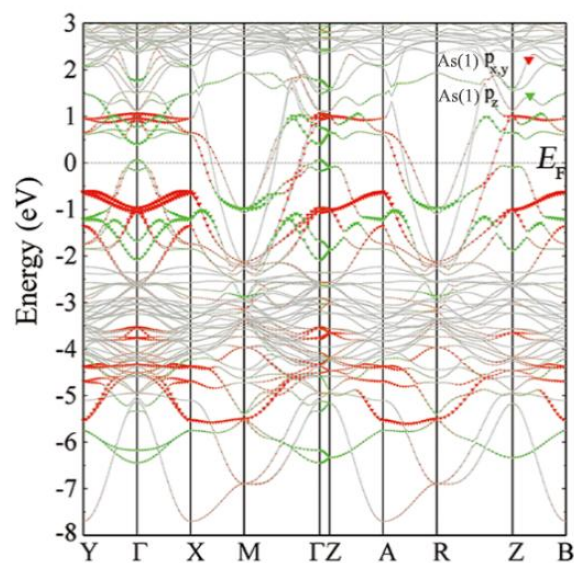

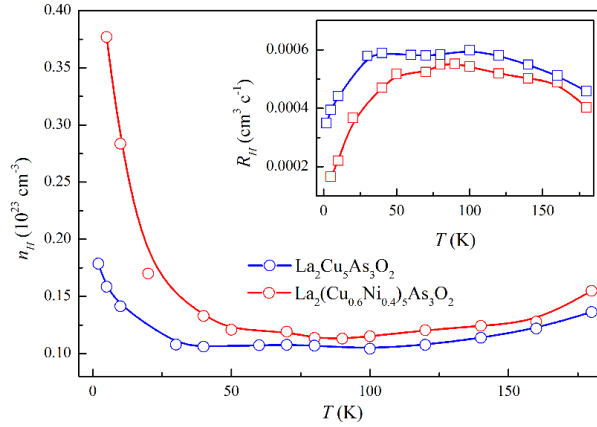**Figure S12.** As(1) P$_{x,y}$ and P$_z$ orbital-resolved band structure. Related to Figure 5.

Figure S13. The carriers concentrations of $La_2Cu_5As_3O_2$ and $La_2(Cu_{0.6}Ni_{0.4})_5As_3O_2$ measured from 5 K-180 K. Inset shows the Hall coefficients. Related to Figure 5.
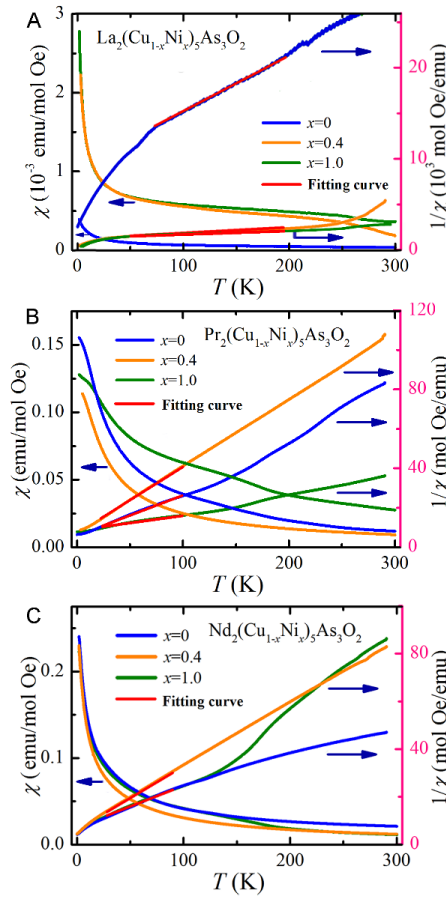

Figure S14. Temperature-dependent of normal-state susceptibility (χ) and $1/\chi$ for $La_2(Cu_{1-x}Ni_x)_5As_3O_2$ ($x=0$, $\mu_{eff}=0.16$ μ_B per Cu; $\theta=-148$ K; $x=0.4$, $\mu_{eff}=0.56$ μ_B per Cu; $\theta=-256$ K; $x=1.0$, $\mu_{eff}=0.69\mu_B$ per Cu; $\theta=-424$ K) (A), $Pr_2(Cu_{1-x}Ni_x)_5As_3O_2$ ($x=0$, $\mu_{eff}=4.42$ μ_B per Pr; $\theta=-26.5$ K; $x=0.4$, $\mu_{eff}=3.48$ μ_B per Pr; $\theta=-19.5$ K; $x=1.0$, $\mu_{eff}=6.26\mu_B$ per Pr; $\theta=-70.1$ K) (B) and $Nd_2(Cu_{1-x}Ni_x)_5As_3O_2$ ($x=0$, $\mu_{eff}=4.62$ μ_B per Nd; $\theta=-30.4$ K; $x=0.4$, $\mu_{eff}=2.75$ μ_B per Nd; $\theta=-21.9$ K; $x=1.0$, $\mu_{eff}=4.73\mu_B$ per Nd; $\theta=-36.4$ K) (C). Data can be well fitted by Curie-Weiss equation, and the fitting results are shown in the inset. The fitting curves are drawn as red lines. Related to Figure 5.

Transparent Methods

Synthesis:

Polycrystalline samples of $RE_2(Cu_{1-x}Ni_x)_5As_3O_2$ (x=0.0-1.0) were synthesized by solid state reactions. The binary precursors REAs (RE=La, Pr, Nd), Cu_3As and NiAs were pre-synthesized by reacting La filings, Cu, Ni and As powders at 1000 K for 20 h. Then, the powders of REAs, Cu_3As, NiAs, La_2O_3, Ni and Cu were weighted as the stoichiometric ratio, ground and pelleted under a pressure of 50 MPa in an argon-filled glove box. The pellets were loaded into an Al_2O_3 crucible and sealed into evacuated silica tube, which was heated up to 1250 K and kept for 40 h.

Characterization:

The powder X-ray diffraction (PXRD) pattern was collected at room temperature using a Panalytical diffractometer (Cu K_α radiation) equipped a low-temperature option (10 K-300 K). Rietveld refinements were performed using Fullprof suites (**Rodríguez, 1990**). The composition of the sample was determined by Energy Dispersive Spectroscopy (EDS). The real composition was averaged as 10 sets of data. The high-angle annular-dark-field (HAADF) image was obtained using an ARM-200F (JEOL, Tokyo, Japan) scanning transmission electron microscope (STEM) operated at 200 kV with a CEOS Cs corrector (CEOS GmbH, Heidelberg, Germany) to cope with the probe-forming objective spherical aberration. The attainable resolution of the probe defined by the objective pre-field is 78 picometers. The low-temperature STEM images were taken using an ARM-200F (JEOL, Tokyo, Japan) equipped a side-entry liquid-He stage. The electrical resistivity (ρ), dc magnetic susceptibility (χ) and specific heat (C_p) were measured through the standard four-wire method (PPMS, Quantum Design) and SQUID (MPMS, Quantum Design), respectively. The resistivity and specific heat below 1.8 K were measured in an Oxford fridge equipped with a dilution refrigerator and a He-3 probe. We attached the electrodes in the glove box and protected the samples by using N-grease to avoid oxidation.

DFT Calculations:

Our calculations are performed using density functional theory (DFT) as implemented in the Vienna *ab* initio simulation package (VASP) code (**Kresse and Hafner, 1993; Kresse and Furthmuller, 1996; Kresse and Furthmuller, 1996**). The Perdew-Burke-Ernzerhof (PBE) exchange-correlation functional and the projector-augmented-wave (PAW) approach are used. Throughout the work, the cutoff energy is set to be 550 eV for expanding the wave functions into plane wave basis. The Brillouin zone is sampled in the k space within Monkhorst-Pack scheme (**Monkhorst and Pack, 1976**). On the basis of the equilibrium structure, the k mesh used is 4×4×4 and 10× 10×2 for primitive and conventional cell, respectively. In our calculations, we adopt the experimental structural parameters of $La_2Cu_5As_3O_2$.

Rodríguez, C. (1990). J. Fullprof: a program for Rietveld refinement and pattern matching analysis. *Abstract of the Satellite Meeting on Powder Diffraction of the XV Congress of the IUCr*, (Toulouse, France).

Kresse, G., and Hafner, J. (1993). *Ab* initio molecular dynamics for liquid metal. Phys. Rev. B *47*, 558.

Kresse, G., and Furthmuller, J. (1996). Efficiency of *ab*-initio total energy calculations for metals and semiconductors using a plane-wave basis set. Comput. Mater. Sci. *6*, 15-60.

Kresse, G., and Furthmuller, J. (1996). Efficient iterative schemes for *ab* initio total-energy calculations using a plane-wave basis set. Phys. Rev. B *54*, 11169.

Monkhorst, H.J., and Pack, J. (1976). Special points for Brillouin-zone integrations. Phys. Rev. B *13*, 5188.